Int J Fract (2012) 177:141–162
DOI 10.1007/s10704-012-9760-9

ORIGINAL PAPER

# A new mechanism in hydrogen-enhanced fatigue crack growth behavior of a 1900-MPa-class high-strength steel

**Junichiro Yamabe · Takuya Matsumoto · Saburo Matsuoka · Yukitaka Murakami**

Received: 9 September 2011 / Accepted: 24 July 2012 / Published online: 17 August 2012
© Springer Science+Business Media B.V. 2012

**Abstract** This paper presents a new mechanism controlling the acceleration of fatigue crack growth of a hydrogen-charged high-strength steel (bearing steel SAE52100, $\sigma_{ult} > 1,900$ MPa, $HV = 569$). Three-dimensionally complicated shape of a primary crack and secondary cracks were observed in hydrogen-charged specimens. Marked acceleration of fatigue crack growth in the presence of hydrogen was observed particularly at low test frequency, and was attributed to the initiation and successive coalescence of secondary cracks formed ahead of primary crack. These secondary cracks were produced along prior-austenite grain boundaries and carbide boundaries, or by direct cracking of carbides. Surprisingly, secondary cracks were observed outside the ordinary plastic zone ahead of the crack tip. TEM observation elucidated that the secondary cracks outside the crack tip plastic zone were produced by hydrogen-induced deformation twins impinging on grain boundaries and carbides. These results suggest a new mechanism of the acceleration of fatigue crack growth rates in high-strength steels caused by hydrogen-induced deformation twins, rather than due to hydrogen-enhanced localized plasticity. The phenomena associated with time dependent fatigue crack growth are presumed to be correlated with the initiation and coalescence of secondary cracks in the presence of hydrogen.

**Keywords** Hydrogen embrittlement · Fatigue crack growth · High-strength steel · Deformation twin · Intergranular fracture · Time dependent fracture

J. Yamabe · S. Matsuoka · Y. Murakami (✉)
International Institute for Carbon-Neutral Energy Research (WPI-I$^2$ CNER), Kyushu University, 744 Moto-oka, Nishi-ku, Fukuoka 819-0395, Japan
e-mail: murakami.yukitaka.600@m.kyushu-u.ac.jp

J. Yamabe · S. Matsuoka · Y. Murakami
Research Center for Hydrogen Industrial Use and Storage (HYDROGENIUS), National Institute of Advanced Industrial Science and Technology (AIST), 744 Moto-oka, Nishi-ku, Fukuoka 819-0395, Japan

J. Yamabe
International Research Center for Hydrogen Energy, Kyushu University, 744 Moto-oka, Nishi-ku, Fukuoka 819-0395, Japan

T. Matsumoto
Graduate School of Engineering, Kyushu University, 744 Moto-oka, Nishi-ku, Fukuoka 819-0395, Japan

S. Matsuoka
Department of Mechanical Engineering, Kyushu University, 744 Moto-oka, Nishi-ku, Fukuoka 819-0395, Japan

## 1 Introduction

It is well known that hydrogen, either in gaseous form, internally charged, or in a hydrogen-producing environment, can result in severe deterioration of the material properties of steels, and in particular in high-strength steels with static strength exceeding ~1 GPa (Walter and Chandler 1968; Sandoz 1972; Chandler

and Walter 1974, 1975; Fujita and Yamada 1977; Toplosky and Ritchie 1981; Bandyopadhyay et al. 1983; Tau et al. 1996; Gangloff 2003; Marchi and Somerday 2008; Kondo et al. 2010). Recent demands to understand the mechanism of hydrogen embrittlement for developing the so called "Hydrogen Economy" include more pressing technical problems. One important task for mechanical engineers and material scientists is the development of materials and systems which are capable of withstanding the effects of cyclic loading in hydrogen environments.

In the past much research has been concentrated on the phenomenon known as hydrogen embrittlement (HE) (Farrell and Quarrell 1964; Shih et al. 1988; Brass and Chene 1998). Hydrogen effects on slip localization (Shih et al. 1988; Brass and Chene 1998; Birnbaum and Sofronis 1994), softening and hardening (Heller 1961; Au and Birnbaum 1973; Dufresne et al. 1976; Matsui et al. 1979; Kimura and Matsui 1979; Hirth 1980; Birnbaum and Sofronis 1994; Senkov and Jonas 1996; Magnin et al. 2001), hydrogen-dislocation interactions (Clum 1975; Birnbaum et al. 2000; Magnin et al. 2001), and creep (Mignot et al. 2004) have been also reported. However, most research on HE over the past 40 years has paid insufficient attention to two points that are crucially important in the elucidation of the true mechanism. One is that, in most studies, the hydrogen content of specimens was not directly measured. For crack-growth tests conducted in hydrogen gas, the hydrogen concentration cannot be easily measured. Therefore, for the time being, we cannot help applying a principle of similitude to the crack tip environment, e.g., for equal levels of hydrogen gas fugacity and crack-tip stress/strain fields, there are equal levels of hydrogen embrittlement. Second, detailed studies that quantified the influence of hydrogen on fatigue crack growth behavior based on microscopic observations of crack tip morphology are very rare; many studies have focused on the influence of hydrogen on fracture phenomena under monotonic or sustained loading (Troiano 1960; Vennett and Ansell 1967; Benson et al. 1968; Lagneborg 1969; Beachem 1972; Oriani and Josephic 1974; Garber et al. 1976; Cialone and Asaro 1979; Eliezer et al. 1979; Rosenthal et al. 1981; Singh and Altstetter 1982; Stoltz et al. 1983; Tabata and Birnbaum 1983; Robertson and Birnbaum 1986; Rozenak et al. 1990; Ferreira et al. 1998; Valiente et al. 1999; Nagumo et al. 2001), though less studies on fatigue properties in the presence of hydrogen have been reported (Suresh and Ritchie 1982; Murakami et al. 1999, 2000, 2010; Murakami 2002; Kawazoe et al. 2005, personal communication; Kanezaki et al. (2008)). Furthermore, it is known that fatigue properties of high-strength steels in the presence of hydrogen are time dependent (Wei and Landes 1969; Endo et al. 1980; Somerday and March 2008; Knop et al. 2010; Kondo et al. 2010). Even in low-strength steels (Murakami et al. 2008; Matsuoka et al. 2010; Yoshikawa et al. 2010; Matsuoka et al. 2011; Macadre et al. 2011a), the fatigue crack growth rate is strongly dependent on cyclic frequency. The ratio of static strength in the presence of hydrogen to that in air drastically drops at static strength levels exceeding ~1 GPa (Walter and Chandler 1968; Sandoz 1972; Chandler and Walter 1974, 1975; Fujita and Yamada 1977; Bandyopadhyay et al. 1983; Gangloff 2003; Marchi and Somerday 2008). Drastic acceleration of the fatigue crack growth rate is also observed in high-strength steels with strength levels exceeding ~1 GPa (Kondo et al. 2010). Regarding the acceleration of the fatigue crack growth in the presence of hydrogen for high-strength steels, the superposition models of mechanical fatigue crack and sustained-load crack were reported from 1960s to 1980s (Wei and Landes 1969; Wei and Simmons 1981; Suresh and Ritchie 1982). However, the microscopic mechanism of these phenomena has not been elucidated so far, though a few models for explaining the phenomena have been proposed (Kameda and McMahon 1980; Novak et al. 2010). In order to produce components of high-strength steels which must be used safely in service for up to 15 years, there is an urgent need for understanding the basic mechanism of the acceleration of fatigue crack growth rate, and time dependent fracture.

Extensive studies by the author's group on the effect of hydrogen on fatigue crack growth behavior in low-strength steels (Murakami et al. 2008; Murakami et al. 2010; Matsuoka et al. 2010; Yoshikawa et al. 2010; Murakami and Matsuoka 2010; Matsuoka et al. 2011; Macadre et al. 2011a) have quantified that the acceleration and strong frequency dependence of fatigue crack growth are basically related to the hydrogen-enhanced localized plasticity (HELP) mechanism (Sofronis and McMeeking 1989; Birnbaum and Sofronis 1994). In contrast, high-strength steels show a severe deterioration of tensile strength (Walter and Chandler 1968; Sandoz 1972; Chandler and Walter 1974, 1975; Fujita and Yamada 1977; Bandyopadhyay et al. 1983; Gangloff 2003; Marchi and Somerday 2008) and fatigue crack

growth properties (Toplosky and Ritchie 1981; Tau et al. 1996; Kondo et al. 2010) in the presence of hydrogen compared with low-strength steels. A transition of fatigue fracture surface morphology from transgranular (TG) to intergranular (IG) cracking is often observed for high-strength steels in presence of hydrogen (Toplosky and Ritchie 1981; Tau et al. 1996; Kondo et al. 2010), and similar hydrogen-assisted intergranular cracking is also observed in lower strength steels (Suresh and Ritchie 1982). Such hydrogen-induced intergranular cracking is explained in terms of the decrease in cohesion strength of the grain boundary by hydrogen (Yoshino and McMahon 1974; Kameda and McMahon 1980, 1983; Kameda and Jokl 1982; McMahon 2001). Therefore, it is presumed that the mechanism of hydrogen embrittelment for high-strength steels with IG cracking is not identical to that for low-strength steels. Kameda and McMahon (1980) and Novak et al. (2010) explained IG cracking in high-strength steels by a decohesion model based on impingement of dislocation pile-up on the carbide boundary. Liu (2011) discussed a mixture of general mechanisms such as cleavage of grain boundaries and interface decohesion at grain-boundary carbides for IG cracking.

It is presumed that the effects of hydrogen, cyclic frequency, time dependency, microstructures of high-strength steels, and applied stress levels on fatigue crack growth rate acceleration should be mutually coupled. In this paper, the effect of hydrogen on the fatigue crack growth behavior of a high-strength steel (bearing steel SAE52100, $\sigma_{\mathrm{ult}} > 1{,}900$ MPa, $HV = 569$) was investigated based on precise experiments and microscopic observations. First, fatigue tests were conducted at different frequencies ($f$), i.e. $f = 0.2$, 2 and 20 Hz. Next, in order to investigate the frequency effect, two-step fatigue tests were conducted with the first step at $f = 0.02, 0.2$, or 2 Hz, and then the test frequency was switched for the second step to 20 Hz. Before the start of the second step test, secondary cracks which were formed during the first step test were observed ahead of the primary crack by a field emission scanning electron microscope (FE-SEM). Finite element analysis was carried out to clarify the relationship between the locations of secondary cracks, the ordinary plastic zone, and hydrostatic stress. The microstructural mechanism of the acceleration of fatigue crack growth by hydrogen in relation to fracture surfaces was investigated with a FE-SEM and a field emission transmission electron microscope (FE-TEM). This detailed microscopic information on the fatigue crack tip at the end of the first step test of lower test frequency and before the second step test of higher test frequency, and fatigue crack growth measurements have revealed a new mechanism of the acceleration of the fatigue crack growth rate due to hydrogen.

## 2 Material and experimental methods

### 2.1 Material and specimens

Cylindrical bars of bearing steel SAE52100 were used for test specimens. Table 1 shows the chemical composition of this bearing steel. Figure 1a shows the orientation of a wedge opening load (WOL) specimen. Figure 1b shows the final geometry of the WOL specimen. Cylindrical bars 88 mm in diameter were firstly pre-machined. These pre-machined specimens were approximately 1 mm larger than the final size. The pre-machined specimens were oil-quenched from 1,113 K, followed by tempering at 643 K, and subsequently machined to the dimensions shown in Fig. 1b. Specimen surfaces were finished by buffing after polishing with #2000 emery paper.

Figure 2a shows the microstructure of the cylindrical bar. On a longitudinal cross-section of the bar, alternate layers of an optically black (B) layer and an optically white (W) layer can be seen. Figure 2b shows a high magnification view of the longitudinal microstructure. More longitudinal non-metallic inclusions exist in the B layer than in the W layer. Figure 2c, d show high magnification views of the B layer and the W layer. The prior austenite grain size in the W layer is larger than that in the B layer. More carbides exist in the B layer than in the W layer. It will be explained later that the difference in grain size between the B layer and the W layer existing in the same specimen quantifies by chance the effect of grain size on the different crack growth path morphologies, i.e., transgranular (TG), or intergranular (IG) cracking.

Vickers hardness was measured on the longitudinal cross section of the bar with a measurement load of 1.94 N. The hardness of the B layer was *HV*585 averaged over 10 measurements (scatter: ±4 %), and the hardness of the W layer was *HV*553 averaged over 10 measurements (scatter: ± 2 %). Tensile properties in the longitudinal direction were evaluated by using a cylindrical bar specimen with a diameter of 4.5 mm. The

**Table 1** Chemical composition (mass%, * mass ppm)

| Material | C | Si | Mn | P | S | Cu | Ni | Cr | Mo | O* |
|---|---|---|---|---|---|---|---|---|---|---|
| SAE52100 | 1.00 | 0.18 | 0.40 | 0.018 | 0.006 | 0.11 | 0.06 | 1.40 | 0.03 | 5 |

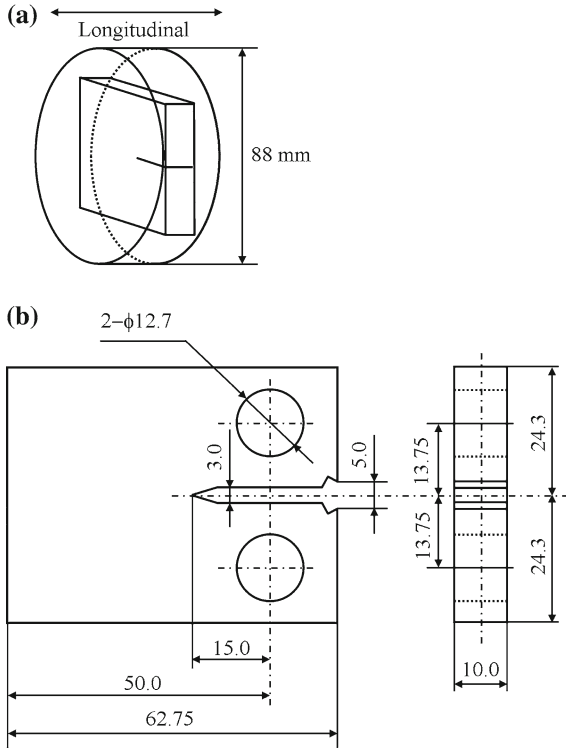


**Fig. 1** Specimen orientation, shape, and dimensions of the WOL specimen, in mm: **a** specimen orientation; **b** WOL specimen

tensile test was conducted under a cross head speed of 1 mm/min at room temperature in laboratory air. Figure 3 shows the nominal stress–strain curve of the cylindrical bar specimen. The fracture originated from an inclusion (TiN) with a size of 10 μm. The 0.2 % proof strength $\sigma_{0.2}$ is 1,794 MPa, and the nominal fracture strength $\sigma_F$ is 1,928 MPa. Therefore, the true ultimate tensile strength $\sigma_{ult}$ without the influence of inclusions is estimated to be higher than 1,900 MPa.

## 2.2 Hydrogen charging and hydrogen content measurement

Hydrogen charging was carried out by exposing test specimens to high-pressure hydrogen gas at 100 MPa and a temperature of 358 K for 200 h, before fatigue crack growth tests at room temperature in laboratory air. However, in the case of the material studied here with a martensitic structure, hydrogen diffuses out of the specimens during the tests. Ductility and fatigue crack growth rate vary with hydrogen content in material (Takai and Watanuki 2003; Matsuo et al. 2009; Murakami et al. 2010; Yano et al. 2010). Therefore, it is necessary to identify the variation of hydrogen content of the specimens during the tests. In this study, reference specimens with dimensions of 20 mm × 10 mm × 62.75 mm heat-treated under the same conditions as the WOL specimen were prepared for estimating the hydrogen content during fatigue testing. We call this the hydrogen content measurement (HCM) specimen. The HCM specimen was hydrogen-charged under the same conditions as the WOL specimen, and then exposed to the same laboratory conditions as the fatigue crack growth test. At given time intervals, strip samples with a size of 2 mm × 10 mm × 3 mm were cut from the HCM specimen. Similar samples were also cut from the WOL specimens after fatigue tests. The hydrogen content was measured using thermal desorption spectrometry (TDS) up to 573 K, at a heating rate of 0.5 K/s.

## 2.3 Fatigue crack growth test

### *2.3.1 Measurement of crack length*

Fatigue crack growth tests were performed at room temperature in laboratory air under a sine wave cyclic loading. The stress ratios ($R$ = minimum load/maximum load) were $R = 0.1$ and 0.5, and test frequencies were $f = 0.2$, 2, and 20 Hz. $\Delta K$-increasing tests and $\Delta K$-decreasing tests were carried out. The $\Delta K$-increasing tests with crack growth were carried out under constant-amplitude loading. The $\Delta K$-decreasing tests were carried out by shedding load, either continuously or by a series of decremental steps with crack growth. The step-by-step reduction of load was controlled within 4–10 % according to ASTM-E647 (2010).

Crack length was indirectly measured by the compliance method (ASTM 2010), using crack-opening displacement (COD) at the front face of the WOL

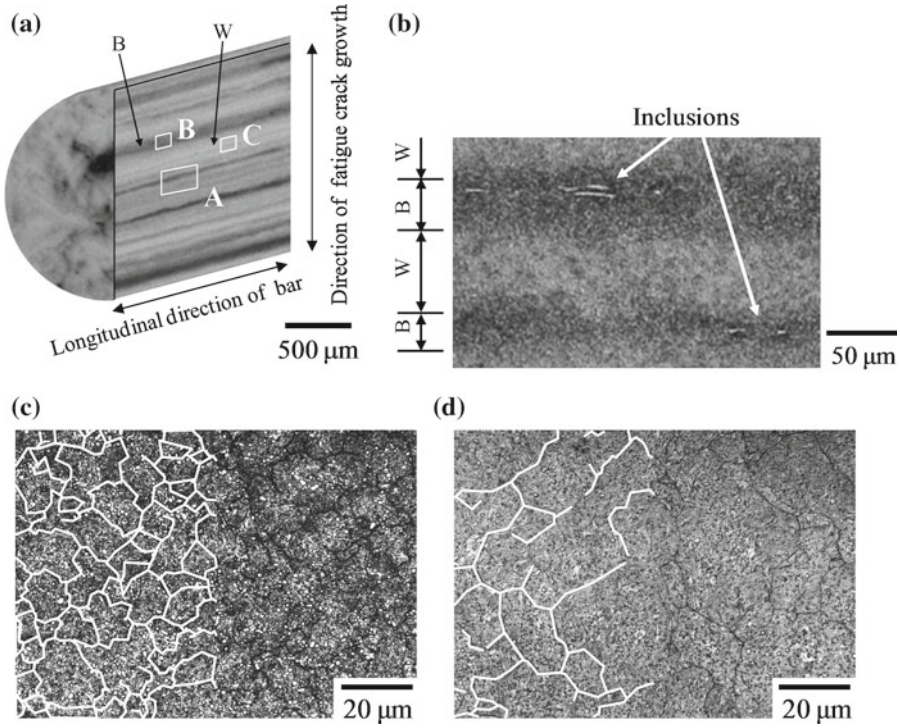


**Fig. 2** Microstructure of material: **a** microstructure of bar; **b** magnification of region A; **c** magnification of region B (*black layer*); **d** microstructure of region C (*white layer*). The *white lines* in **c** and **d** show prior austenitic grain boundary. More carbides and smaller prior austenite grains were observed in the B layer than in the W layer

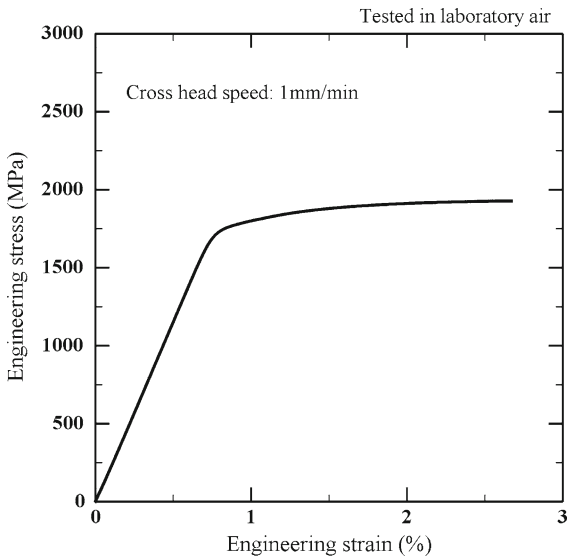


**Fig. 3** Engineering stress–strain curve obtained from tensile test

specimen. In order to calibrate the relationship between crack length and compliance at the front face of the WOL specimen, a beach-mark test was carried out. Observing crack front marks left on the fatigue fracture surface by the beach-mark test, the average crack length considering the curvature of the crack front marks was determined, and the following calibration relationship was experimentally obtained:

$$a/W = 4.6694 - 198.45U_0 + 4055(U_0)^2 - 41742(U_0)^3 + 210458(U_0)^4 - 416467(U_0)^5 \quad (1)$$

$$U_0 = \frac{1}{\left(\frac{BEV_0}{P}\right)^{1/2} + 1} \quad (2)$$

where $a$ crack length, $W$ specimen width, $B$ specimen thickness, $E$ Young's modulus, $V_0$ COD at the front face of the WOL specimen, $P$ load, $(BEV_0)/P$ compliance at the front face of the WOL specimen. The stress intensity factor range $\Delta K$ was calculated by Eq. (3) (Murakami editor-in-chier 1987):

$$\Delta K = \frac{\Delta P(2+\alpha)}{B\sqrt{W}(1-\alpha)^{3/2}}(0.8072 + 8.858\alpha - 30.23\alpha^2 + 41.088\alpha^3 - 24.15\alpha^4 + 4.951\alpha^5) \quad (3)$$

where $\alpha = a / W$ and $\Delta P$ is load range.

### 2.3.2 Tests for identifying frequency effect

In addition to the ordinary fatigue crack growth tests under constant frequencies of 0.2, 2, and 20 Hz, special

fatigue crack growth tests were carried out to investigate the frequency effect by hydrogen. In this test, the frequency was switched from 0.02 to 20 Hz, from 0.2 to 20 Hz, and from 2 to 20 Hz, using hydrogen-charged specimens.

### 2.4 Observations by SEM and TEM

Fatigue crack morphology was observed by the FE-SEM. The FE-SEM was used for clarifying the difference in the morphology of fracture surfaces between the uncharged and hydrogen-charged specimens.

For FE-TEM observations, cutting a cross section perpendicular to the fracture surface in the direction of subsurface by the focused ion beam (FIB) technique, a thin film was prepared. Carbon was deposited on the surface of the thin film, and then the thin film was investigated using FE-TEM to identify the microstructure of the zone just beneath the IG fracture surface.

### 2.5 Analysis of plastic zone and hydrostatic stress ahead of the primary crack by Finite element method (FEM)

Finite element method (FEM) was employed for calculating the ordinary plastic zone and the hydrostatic tensile stress ahead of the primary crack. Figure 4a shows a FEM model of the WOL specimen shown in Fig. 2, constructed by using eight-node quadrilateral elements. The minimum element size at the primary crack tip was set to 0.1 μm. The FEM calculation was conducted assuming plane strain condition without considering secondary cracks ahead of the primary crack by using the commercial code (ANSYS Ver. 11).

Figure 4b shows the engineering stress–strain curve ($\sigma$–$\varepsilon$ curve) modified for the FEM analysis from the engineering stress–strain curve shown in Fig. 3. It has been reported that the $\sigma$–$\varepsilon$ curve of a high-strength bearing steel shows a cyclic softening (Smith et al. 1963; Hahn et al. 1990), and that the 0.2 % proof strength $\sigma_{0.2}$ of a cyclic $\sigma$–$\varepsilon$ curve is about 40 % lower than that of a monotonic $\sigma$–$\varepsilon$ curve in bearing steel ($\sigma_{0.2} = 1,922$ MPa, $\sigma_F = 2,012$ MPa) (Smith et al. 1963). Considering cyclic softening of the high-strength steel used in this study ($HV = 569$, $\sigma_{0.2} = 1,794$ MPa, $\sigma_F = 1,928$ MPa), the modified cyclic $\sigma - \varepsilon$ curve shown in Fig. 4b was used for the calculation. Since

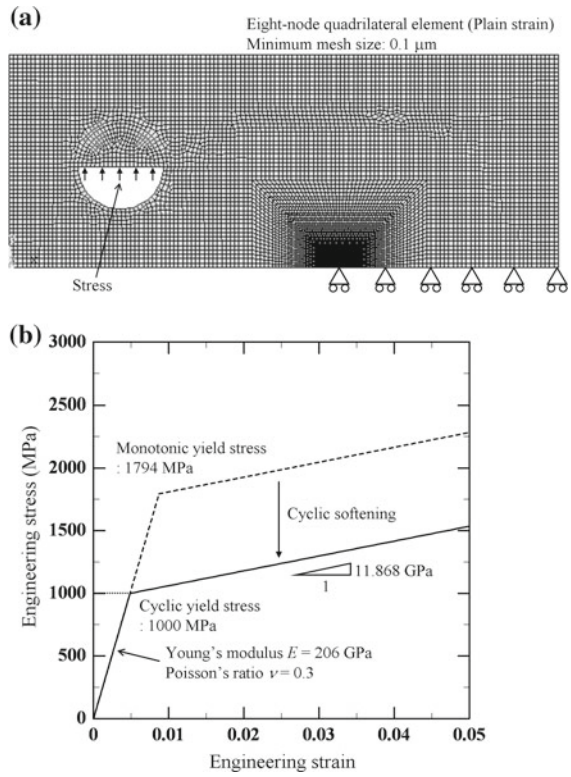


**Fig. 4** FEM model of WOL specimen and engineering stress–strain curve for FEM analysis: **a** FEM model of the WOL specimen; **b** relationship between engineering stress and strain for FEM analysis

the true cyclic $\sigma - \varepsilon$ curve is unknown, the cyclic plastic zone size calculated in this analysis is not exact one but is used for a reference value.

## 3 Results and discussion

### 3.1 Hydrogen desorption properties

Figure 5 shows the hydrogen desorption profiles of uncharged and hydrogen-charged specimens. The hydrogen-charged specimen contains hydrogen with three peaks, which are two distinct peaks at about 430 K (peak 1) and 670 K (peak 2), and a shoulder associated with a small peak (peak3) (Novak et al. 2010), while the uncharged specimen only contains hydrogen at peak 2. Takai and Watanuki (2003) reported that peak 1 hydrogen easily diffuses at room temperature, while peak 2 hydrogen hardly diffuses at room temperature, and that peak 1 hydrogen causes the decrease in ultimate tensile strength and ductility loss in slow strain rate tests

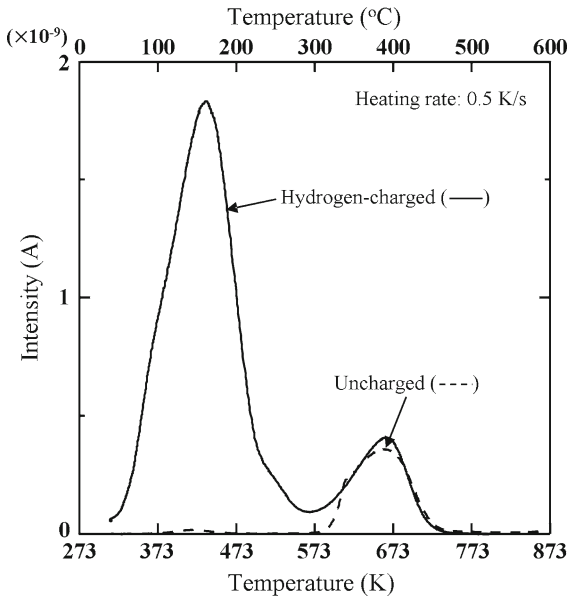


**Fig. 5** Hydrogen desorption profiles by TDS

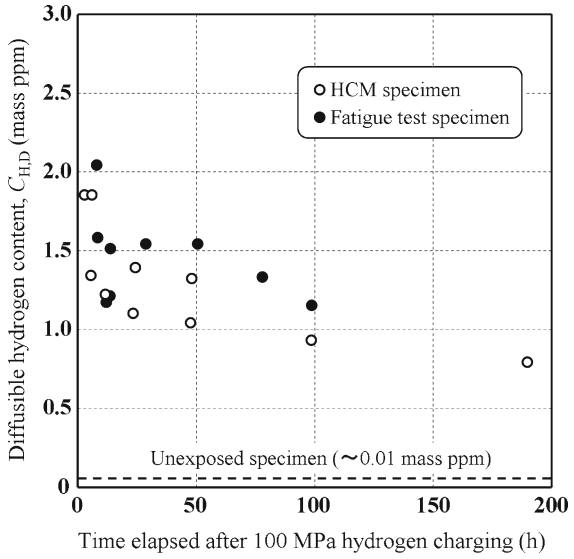


**Fig. 6** Relationship between diffusible hydrogen content, $C_{H,D}$, and time elapsed after 100 MPa hydrogen charging

(SSRT). Therefore, the content of diffusible hydrogen with peak 1 calculated by integrating up to 573 K is termed the *diffusible hydrogen content*, $C_{H,D}$, though this integral includes a slight influence of the hydrogen content for peak 3 in this paper.

Figure 6 shows the relationship between the diffusible hydrogen content $C_{H,D}$ and time elapsed after 100 MPa hydrogen gas charging. The solid circles show the values of $C_{H,D}$ for the WOL specimens after fatigue crack growth tests. The open circles show the hydrogen content measured by using the HCM specimens. The diffusible hydrogen contents in both series of specimens monotonously decreased with time after hydrogen gas charging. The diffusible hydrogen contents in the hydrogen-charged specimens are much higher, even after fatigue crack growth testing (~100 h), than those in the uncharged specimens (approximately 0.01 mass ppm).

## 3.2 Fatigue crack growth behavior

### *3.2.1 Effects of hydrogen and test frequency under constant frequency tests*

Figure 7 shows the relationship between the fatigue crack growth rate d$a$/d$N$ and the stress intensity factor range, $\Delta K$. $C_{H,D}$ is the diffusible hydrogen content measured after the fatigue tests. The fatigue crack growth rates of hydrogen-charged specimens are much faster than those of the uncharged specimens at $R = 0.1$ and 0.5, though the values of d$a$/d$N$ for hydrogen-charged specimens at $\Delta K \approx \Delta K_{th}$ gradually decrease, approaching those of uncharged specimens, with decreasing $\Delta K$. Toplosky and Ritchie (1981) reported the same behavior at near-threshold crack growth rate for ultrahigh-strength steels. The difference in the fatigue crack growth rate at test frequency $f = 0.2$ and 20 Hz at $R = 0.1$ is very small for the uncharged specimens (open symbols). On the other hand, the fatigue crack growth rates of the hydrogen-charged specimens are strongly dependent on test frequency $f$, as shown by the solid symbols at $R = 0.1$.

Figure 8 shows the relationship between the fatigue crack growth rate per unit time, d$a$/d$t$, and the maximum stress intensity factor, $K_{max}$, where d$a$/d$t$ is defined by d$a/dt = f \times$ (d$a$/d$N$), based on the total loading time $1/f$ for one loading cycle (sine wave). The data d$a$/d$t$ of hydrogen-charged specimens for various test frequencies $f$ are likely to converge, though the scatter of the data is still visible due to the variation of stress during one cycle. However, it is evident that the crack growth behavior of the hydrogen-charged high-strength steel (SAE52100, $\sigma_{ult} > 1,900$ MPa, $HV = 569$) displays a time-dependent phenomenon. Thus, for

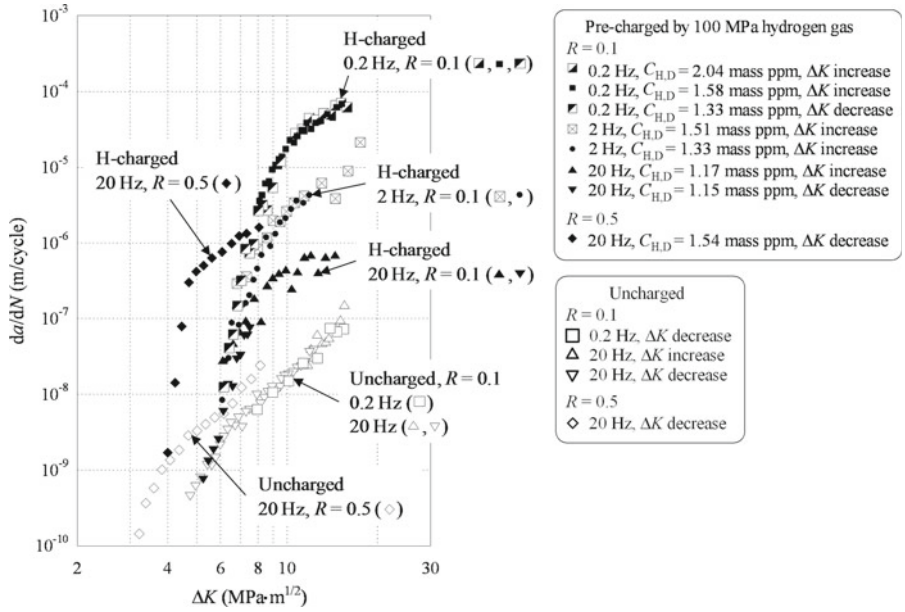


**Fig. 7** Relationship between fatigue crack growth rate, d$a$/d$N$, and stress intensity factor range, $\Delta K$

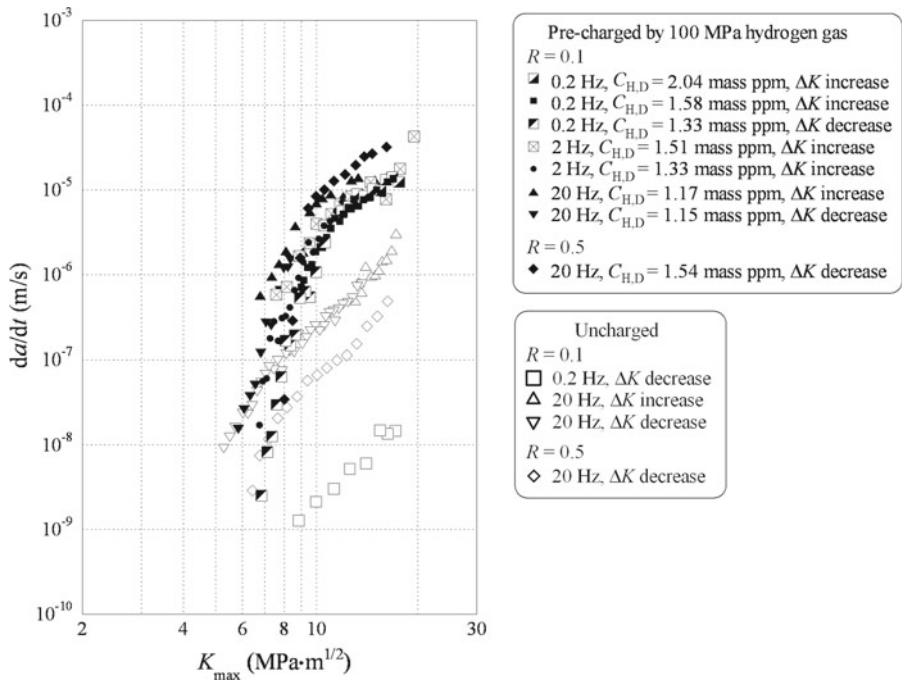


**Fig. 8** Relationship between fatigue crack growth rate per unit time, d$a$/d$t$, and maximum stress intensity factor, $K_{max}$

quantifying the effects of test frequency and $\Delta K$ or $K_{max}$ on the acceleration of fatigue crack growth in the presence of hydrogen in the high-strength steel, the superposition model (Wei and Landes 1969; Wei and Simmons 1981) must be considered.

### *3.2.2 Tests with switching frequency*

In order to investigate the acceleration of fatigue crack growth rate by hydrogen at low test frequency, the test frequency $f$ was switched during the fatigue crack

growth tests of the hydrogen-charged specimens in three series of tests, *i.e.*, Case (a) from 2 to 20 Hz, Case (b) from 0.2 to 20 Hz, and Case (c) from 0.02 to 20 Hz.

Figure 9 shows the relationship between the crack increment $\Delta a$ and the incremental cycles $\Delta N$ after switching test frequency for the hydrogen-charged specimen. The test frequency was switched from 2, 0.2, or 0.02 Hz to 20 Hz at $\Delta K \approx 12\,\mathrm{MPa}\cdot\mathrm{m}^{1/2}$. The crack growth rate was accelerated immediately after switching to $f = 20$ Hz compared with the case of the uncharged specimen. The zone where the crack growth was accelerated is termed a *hydrogen-affected fatigue crack growth zone* (HAFCG zone). The lower the initial frequency before switching $f$ was, the longer the HAFCG zone. The HAFCG zone sizes were; ~40 μm for $f = 2$ Hz, ~75 μm for $f = 0.2$ Hz, and ~143 μm for $f = 0.02$ Hz, at $\Delta K \approx 12\,\mathrm{MPa}\cdot\mathrm{m}^{1/2}$. It follows that the effect of hydrogen is extended more widely ahead of the crack tip at lower frequency.

### 3.3 Initiation of secondary cracks ahead of the primary crack in hydrogen-charged specimens

Figure 10a shows SEM micrographs of the fatigue cracks at the middle section of a hydrogen-charged specimen tested at $f = 0.2$ Hz, $R = 0.1$, and $\Delta K \approx 12\,\mathrm{MPa}\cdot\mathrm{m}^{1/2}$, which is the value of $\Delta K$ at the end of the 0.2 Hz test before switching to 20 Hz. Secondary cracks were observed in all hydrogen-charged specimens, while such secondary cracks were not formed in uncharged specimens tested under the same conditions. All secondary cracks were observed inside the HAFCG zone. However, this is the result obtained by two-dimensional (2D) observation. The fatigue crack in the hydrogen-charged specimens has a three-dimensionally complicated shape, the details of which are shown in Appendix A (Figs. 16, 17, 18). As shown in Fig. 16 of Appendix A, most of these secondary cracks are three-dimensionally (3D) connected to the primary crack. However, secondary cracks, which are completely isolated from the primary crack, are also observed as shown in Figs. 17 and 18 of Appendix A. Considering these crack initiation and growth morphology, we can schematically illustrate the model for successive initiation and coalescence of secondary cracks as Fig. 11.

Figure 10b shows a magnified view of the two-dimensionally isolated cracks of region A in Fig. 10a. These isolated cracks were formed along the prior-austenite grain boundaries (crack A) and carbide boundaries (crack B), or by direct cracking of carbides (crack C). The detailed mechanism of initiation of these cracks will be explained later (Fig. 15). On the other hand, these isolated cracks were not observed near the crack tip at $\Delta K \approx \Delta K_{\mathrm{th}}$, even in hydrogen-charged specimens, where the fatigue crack growth rate $\mathrm{d}a/\mathrm{d}N$ gradually approached the value of $\mathrm{d}a/\mathrm{d}N$ for an uncharged specimen, with decreasing $\Delta K$ value (see Fig. 7). It follows that the irregularly-shaped crack growth from the primary crack and the acceleration of fatigue crack growth in the presence of hydrogen are attributed to the initiation and successive coalescence of secondary cracks formed ahead of the primary crack.

When we observe the influence of hydrogen on crack growth and fracture, the term '*hydrogen embrittlement* (HE)' is commonly used to explain the effect of hydrogen. However, using the term 'HE' to explain the acceleration of crack growth rate or decrease in fracture toughness does not necessarily mean that we understand the reality of the phenomenon such as Fig. 10. It is only a replacement of the reality of a phenomenon by terminology.

### 3.4 Finite element analysis of the plastic zone and distribution of hydrostatic stress ahead of the primary crack

Figure 12a shows the plain strain plastic zone ahead of a newly identified primary crack of the specimen shown in Fig. 10. The locations of the newly identified primary crack and secondary cracks in Fig. 10 were determined from 3D observations of fatigue crack morphology by successive polishing in Appendix A (Fig. 17). The calculation was conducted under $K_{\max} = 13.3\,\mathrm{MPa}\cdot\mathrm{m}^{1/2}$ ($\Delta K = 12\,\mathrm{MPa}\cdot\mathrm{m}^{1/2}$ and $R = 0.1$). The calculated plastic zone is much smaller than the secondary crack zone. It follows that the formation of the secondary crack by hydrogen is not correlated directly to the ordinary plastic deformation at the primary crack tip.

Figure 12b shows the hydrostatic tensile stress distribution ahead of the newly identified primary crack shown in Fig. 10. This calculation was conducted under the same conditions as that in Fig. 12a. The hydrostatic stress shows the maximum value near the primary crack tip, and secondary cracks are observed even at the zone

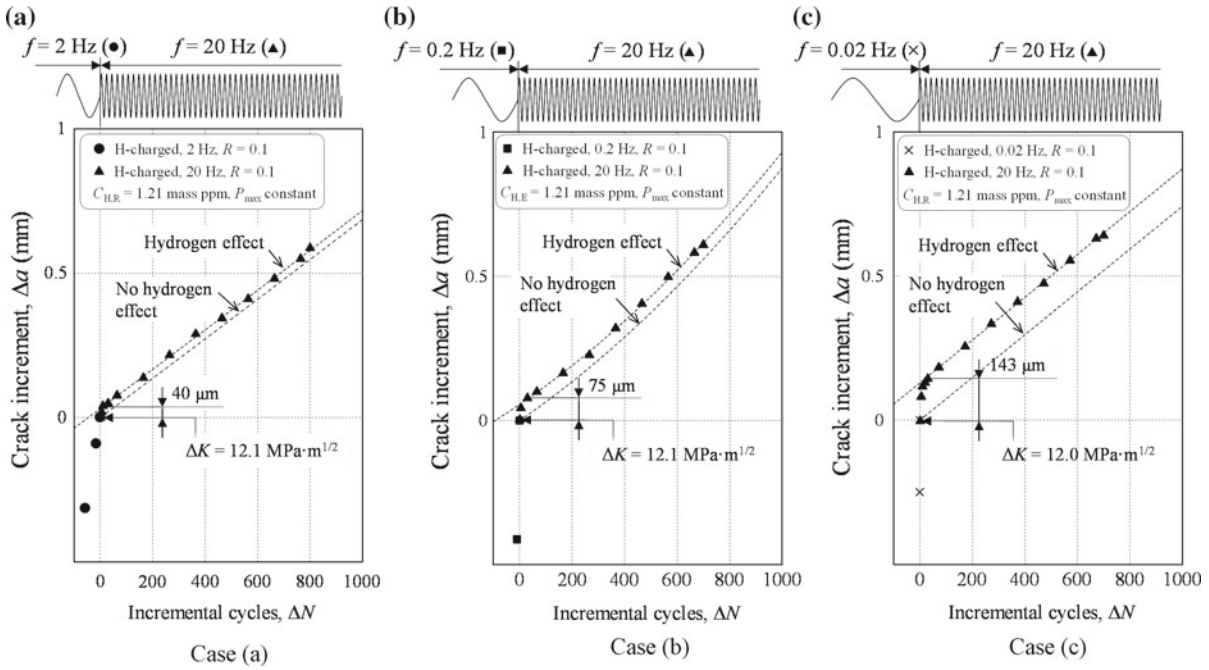


**Fig. 9** Relationship between the crack increment, $\Delta a$, and the incremental cycles, $\Delta N$, for the hydrogen-charged specimen: **a** hydrogen-charged specimen at 2– 20 Hz. A HAFGC zone of 40 μm is formed ahead of the crack tip; **b** hydrogen-charged specimen at 0.2–20 Hz. A HAFGC zone of 75 μm is formed ahead of the crack tip; **c** hydrogen-charged specimen at 0.02–20 Hz. A HAFGC zone of 143 μm is formed ahead of the crack tip

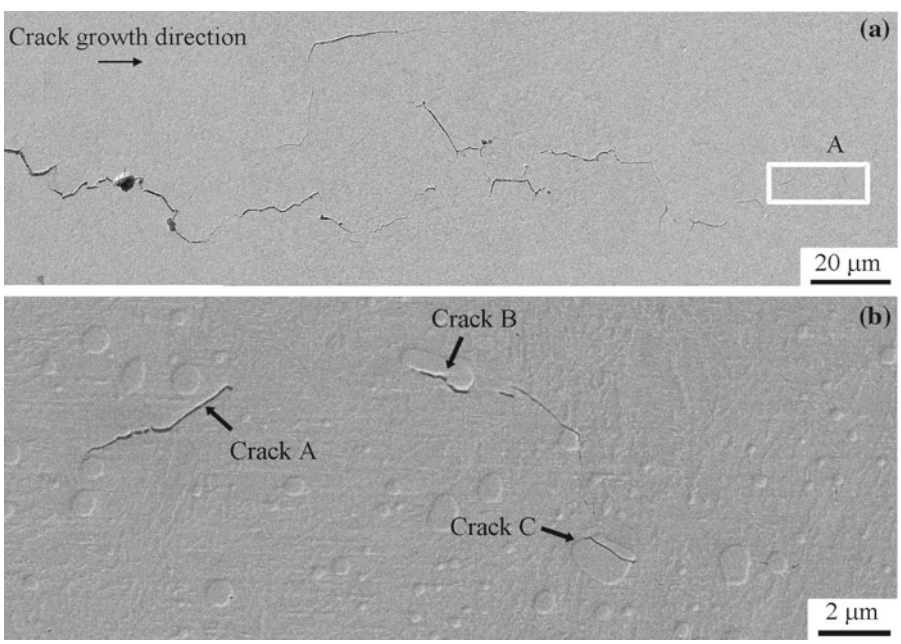


**Fig. 10** SEM micrographs of fatigue cracks at the middle section of a hydrogen-charged specimen ($C_{H,D} = 1.21$ mass ppm, $da/dN \approx 40$ μm/cycle) tested at $f = 0.2$ Hz, $R = 0.1$, $\Delta K = 12.2$ MPa · $m^{1/2}$: **a** low-magnified SEM micrograph; **b** high-magnified micrograph of region A

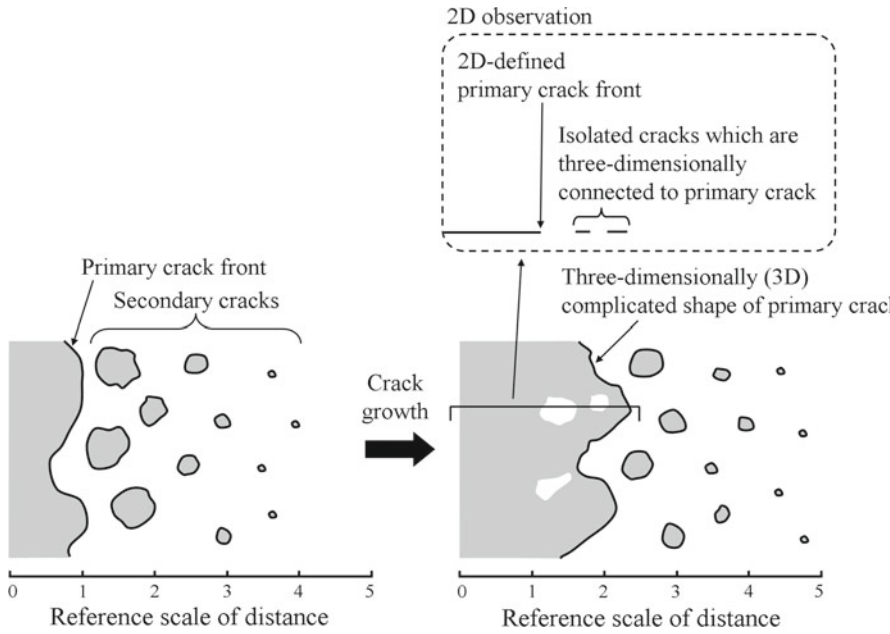


**Fig. 11** Schematic illustration of the model for successive initiation and coalescence of secondary cracks

far from the point of the maximum hydrostatic stress. In this regard, it must be noted that the gradient of hydrostatic tensile stress enhances hydrogen diffusion (Sofronis and McMeeking 1989), and accordingly hydrogen is concentrated ahead of the primary crack with a hydrogen concentration gradient.

The secondary crack zone is much larger than the ordinary plastic zone, and also increases in area with decreasing test frequency $f$. It follows that the initiation of secondary cracks is caused by elastic stress ahead of the primary crack, which occurs at a lower elastic stress at lower test frequency. Hydrogen concentration depends on the time spent for hydrogen diffusion, and there is more time for hydrogen concentration to increase ahead of the primary crack at lower test frequency. It is presumed that that the stress for initiation of secondary cracks decreases with decreasing test frequency $f$, because hydrogen is more concentrated ahead of the primary crack with decreasing $f$. Thus, the fatigue crack growth of hydrogen-charged specimens in relation to the initiation and coalescence of the secondary cracks is time-dependent (Wei and Landes 1969; Endo et al. 1980; Somerday and March 2008; Knop et al. 2010; Kondo et al. 2010), though the mechanism of crack initiation outside the plastic zone is still an unsolved problem.

Suresh and Ritchie (1982) reported the acceleration and deceleration mechanism of the fatigue crack growth rate for a bainitic 2.2.5 Cr–Mo steel tested in hydrogen gas, and the fracture mode change from transgranular (TG) to intergranular (IG). The results presented here show a more drastic coupled effect of hydrogen and frequency, probably because of the higher strength of the material studied here ($\sigma_{ult} > 1{,}900$ MPa, $HV = 569$).

### 3.5 Morphology of fracture surface

The microstructure of the bearing steel used in this study contains an optically black (B) layer and an optically white (W) layer, as shown in Fig. 2. More carbides and smaller prior austenite grains are contained in the B layer than in the W layer.

Figure 13 a-1, b-1 show FE-SEM micrographs of the fracture surfaces of the uncharged and hydrogen-charged specimens tested at 0.2 Hz, $R = 0.1$ and $\Delta K \approx 12\,\mathrm{MPa \cdot m^{1/2}}$, respectively. The boundaries between the B and W layers are indicated by white dashed lines in Fig. 13b-1. TG fracture surfaces are dominant in the uncharged specimen. In the case of the hydrogen-charged specimens, TG fracture surfaces are observed in the B layer with smaller prior austenitic grains, and prior-austenite IG fracture surfaces are observed in the W layer with larger prior austenitic grains. Considering the results reported by Hayakawa et al. (2002), Bechtle et al. (2009), Matsuoka et al. (2010), it is presumed that the microstructure with smaller grains of

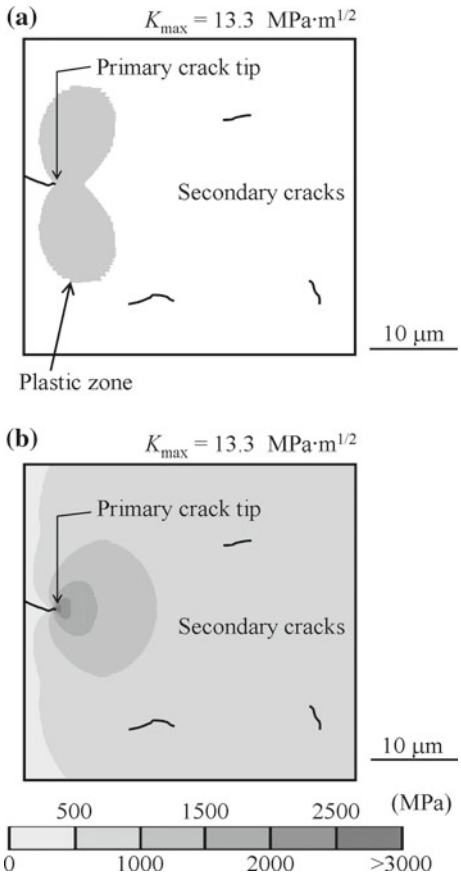


**Fig. 12** Plastic zone and distribution of hydrostatic stress ahead of primary crack without considering secondary cracks in a hydrogen-charged specimen ($C_{H,D}$ = 1.21 mass ppm, d$a$/d$N$ ≈ 40 μm/cycle) tested at $f$ = 0.2 Hz, $R$ = 0.1, $\Delta K$ = 12.2 MPa · m$^{1/2}$: **a** plain strain plastic zone; **b** distribution of hydrostatic stress

this high-strength steel has higher resistance to IG fracture in presence of hydrogen.

Figure 13 a-2, b-2 show magnified views of the TG fracture surfaces of regions A and B in Fig. 13 a-1, b-1 for the uncharged and hydrogen-charged specimens. Many carbides were observed on the TG fracture surface of the hydrogen-charged specimen. The carbides are indicated by arrows in Fig. 13 b-2.

Figure 13 b-3, b-4 show the magnified views of the IG fracture surfaces of regions C and D. The IG fracture surfaces in Fig. 13 b-3, b-4 are not completely smooth, and tear ridges (Beachem 1972) are observed as indicated by arrows in Fig. 13 b-3, b-4. Figure 13 b-5, b-6 show the mating surfaces of Fig. 13 b-3, b-4. Clear tear ridges are not observed on the IG surfaces of Fig. 13 b-5, b-6. The mechanism of formation of the tear ridges will be discussed in the following section on the basis of FE-TEM observations.

### 3.6 Cause of initiation of secondary cracks

The plastic zone calculated by FEM is much smaller than the secondary crack zone as shown in Fig. 12a, and therefore the initiation of secondary cracks is not correlated directly to the ordinary plastic deformation. Therefore, the initiation of the secondary cracks cannot be attributed to the hydrogen-enhanced localized plasticity (HELP) mechanism (Birnbaum and Sofronis 1994; Sofronis and McMeeking 1989). In order to investigate the mechanism of the initiation of secondary cracks, a cross section of the IG fracture surface was observed by FE-TEM for the hydrogen-charged specimen tested under constant frequency at $f$ = 20 Hz, $R$ = 0.1, and $\Delta K \approx 12\,\mathrm{MPa}\cdot\mathrm{m}^{1/2}$.

Figure 14 a-1, a-2 show a pair of the IG fracture surfaces observed by SEM. Linear traces are observed on the IG surface in Fig. 14a-1. The linear traces are almost straight, unlike the curved tear ridges of Fig. 13b-3, b-4. The cross section of the IG surface in Fig. 14a-1 was observed by FE-TEM.

Figure 14b shows a FE-TEM micrograph. Figure 14c shows a magnified view of region A in Fig. 14b. The arrows in Figs. 14b, c indicate microscopic bands in the microstructure. Figure 14d shows the selected area diffraction pattern in the microstructure of Fig. 14c. A double pattern was observed in Fig. 14d. The selected area diffraction pattern indicates that the linear traces in Fig. 14a-1 are the edges of the deformation twins of Fig. 14b, c. Such deformation twins were not observed for uncharged and hydrogen-charged specimens before fatigue test (see Appendix B). It is presumed that the IG fractures of secondary cracks were formed by the stress concentration due to the deformation twins impinging on the prior-austenite boundary or carbide boundary.

Figure 15 illustrates the mechanism for three typical secondary crack initiation modes caused by deformation twins, *i.e.*, IG cracks (crack A in Fig. 10b) (Gilbert et al. 1964), carbide boundary cracks (crack B in Fig. 10b), and carbide cracking (crack C in Fig. 10b). Kameda and McMahon (1980), and Novak et al. (2010) proposed a model for hydrogen-induced intergranular fracture in steel under static bending by assuming a dislocation pile-up impinging on a carbide at a grain boundary and leading to decohesion at a carbide-matrix

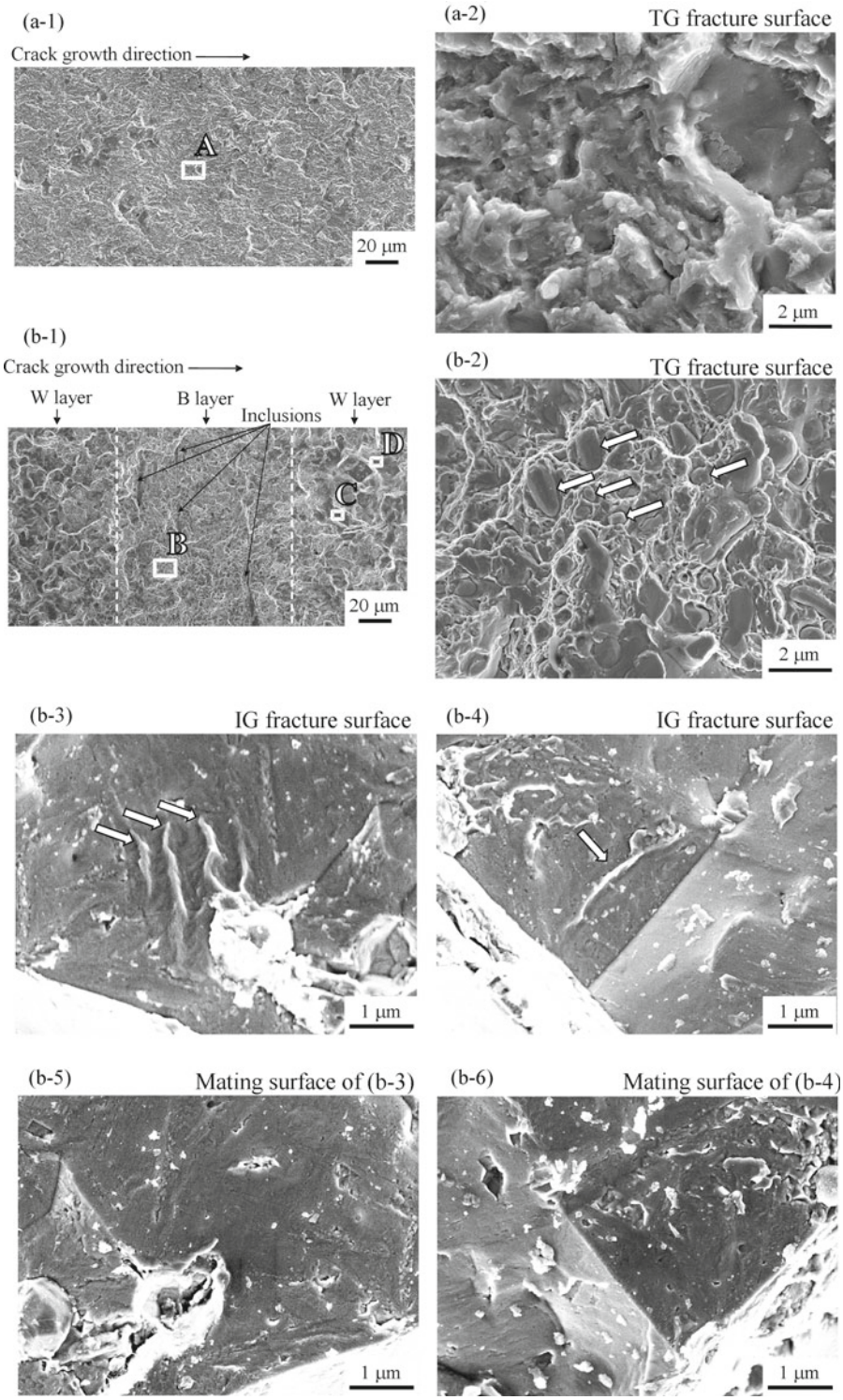


**Fig. 13** Difference in fracture surfaces between uncharged and hydrogen-charged specimens by FE-SEM: **a-1** uncharged specimen ($da/dN \approx 3.5 \times 10^{-2}\,\mu m$/cycle) tested at $f = 0.2\,Hz$, $R = 0.1$, $\Delta K = 12.2\,MPa \cdot m^{1/2}$; **a-2** magnification of region A in (**a-1** ); **b-1** hydrogen-charged specimen ($C_{H,D} = 1.54$ mass ppm, $da/dN \approx 20\,\mu m$/cycle) tested at $f = 0.2\,Hz$, $R = 0.1$, $\Delta K = 10.2\,MPa \cdot m^{1/2}$; **b-2** magnification of region B in (**b-1**). The *arrows* show carbides; **b-3** magnification of region C in (**b-1**). The *arrows* show tear ridges; (b-4) magnification of region D in (**b-1**). The *arrow* shows a tear ridge; **b-5** mating surface of (**b-3**); **b-6** mating surface of (**b-4**)

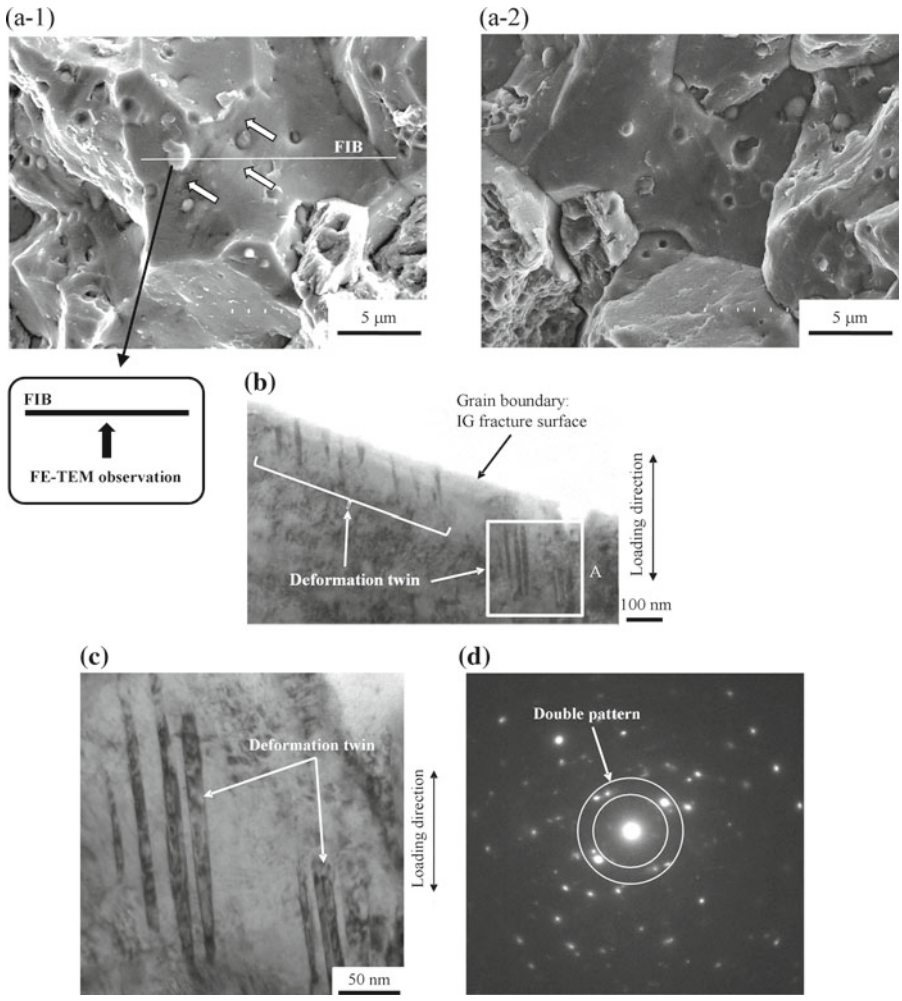


**Fig. 14** FE-TEM micrographs at the cross section of the prior austenite intergranular fracture surface for the hydrogen-charged specimen ($C_{H,D} = 1.17$ mass ppm) tested at $f = 20$ Hz, $R = 0.1$, $\Delta K = 11.6\,\mathrm{MPa} \cdot \mathrm{m}^{1/2}$: **a-1** position of FE-TEM observation. The *arrows* show linear traces. The linear traces are almost straight unlike curved tear ridges; **a-2** mating surface of (**a-1**); **b** FE-TEM micrograph at the cross section of the prior austenite intergranular fracture surface; **c** magnification of A in (**b**); **d** selected area diffraction pattern of (**c**)

interface. However, the secondary cracks observed in this study exist outside the plastic zone ahead of the primary crack, and therefore we can not attribute the initiation of the secondary cracks to pile-up of dislocations impinging on carbides. It is known that the formation of deformation twins is enhanced by hydrogen in some steels and alloys (Rigsbee and Benson 1977; Hwang and Bernstein 1982; Jagannadham et al. 1993; Le et al. 1993; Astafurova et al. 2010), though the role of deformation twins in the initiation of cracks, especially in fatigue, has not been discussed. Figure 14 shows experimental evidence that the decohesion of grain boundaries and carbide boundaries caused by deformation twins outside the plastic zone ahead of the primary crack can be another mechanism for IG fracture.

The linear traces of Fig. 14a-1 are presumed to be the edges of hydrogen-induced deformation twins, which are almost straight, unlike the curved tear ridges shown in Fig. 13b-3, b-4. It is natural to assume that these hydrogen-induced deformation twins cause an array of small IG cracks, as illustrated in Fig. 15a. In this model, subsequently, due to the stress concentration between these small IG cracks, an overall IG fracture surface is formed by coalescence of these small IG cracks. It is presumed that the formation of tear ridges is a consequence of plastic deformation near a grain boundary, caused by the stress concentration between small IG cracks. These tear ridges are observed on only one side of the IG fracture surfaces due to the difference in ease of plastic deformation between two mating grains

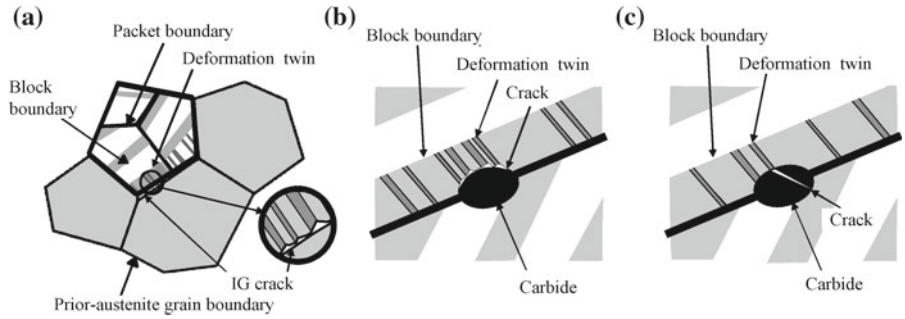


**Fig. 15** Schematic illustration of formation of **a** IG crack, **b** carbide boundary crack, and **c** carbide cracking due to stress concentration by deformation twins: **a** IG crack (crack A in Fig. 10b); **b** carbide boundary crack (crack B in Fig. 10b); **c** carbide cracking due to stress concentration (crack C in Fig. 10b)

having different orientation (compare Fig. 13b-3, b-5, and also Fig. 13b-4, b-6).

## 4 Conclusions

The effect of hydrogen on fatigue crack growth behavior of a high-strength steel (bearing steel SAE52100, $\sigma_{ult} > 1{,}900$ MPa, $HV = 569$) was investigated. The fatigue crack growth tests were carried out at frequencies of $f = 0.2$, 2 and 20 Hz, and with stress ratios of $R = 0.1$ and 0.5, by using uncharged and 100 MPa hydrogen-charged specimens. In order to investigate the time dependency of the effect of hydrogen, special tests in which test frequency $f$ was switched from 0.02, 0.2, or 2 Hz to 20 Hz during the fatigue crack growth test were also conducted on hydrogen-charged specimens. In order to investigate the microstructural mechanism of the acceleration of fatigue crack growth by hydrogen, fracture surfaces were observed with a FE-SEM and a cross section of the fracture surface was observed using a FE-TEM. The conclusions can be summarized as follows.

(1) Fatigue crack growth rate was markedly accelerated by hydrogen. Secondary cracks were observed ahead of the primary crack in hydrogen-charged specimens, but were not observed in uncharged specimens. The crack tip of hydrogen-charged specimens has a three-dimensionally (3D) complicated shape. Although many small isolated cracks were observed by 2D observation ahead of the 2D-defined primary crack, most of these cracks are three-dimensionally connected to the main crack. However, since some small cracks are completely isolated from the primary crack, the 3D-complicated crack shape of hydrogen-charged specimens is thought to be produced by successive initiation and coalescence of isolated secondary cracks. Thus, it is presumed that the acceleration of fatigue crack growth of the hydrogen-charged specimen is caused by the initiation and successive coalescence of the secondary cracks formed ahead of the primary crack.

(2) The fatigue crack growth rate of hydrogen-charged specimens was strongly dependent on test frequency. The dependence on test frequency is a consequence of a larger secondary crack zone produced by decreasing test frequency.

(3) Secondary cracks, though most of them are three-dimensionally connected to the primary cracks, are observed outside the ordinary crack tip plastic zone. Considering the larger zone of secondary crack initiation for lower test frequency, it is presumed that secondary cracks are initiated at a lower stress with decreasing test frequency, which enhances hydrostatic tensile stress-induced hydrogen diffusion and concentration ahead of the primary crack.

(4) Secondary cracks ahead of the primary crack were formed along prior-austenite grain boundaries and carbide boundaries, or by direct cracking of carbides. It is presumed based on precise observation by SEM and TEM that these secondary cracks were produced by hydrogen-induced deformation twins impinging on grain boundaries and carbides. This is a new mechanism of intergranular (IG) cracking under the effect of hydrogen, different from the model of IG cracking produced by pile-up of dislocations impinging on carbides (Kameda and McMahon 1980; Novak et al. 2010).

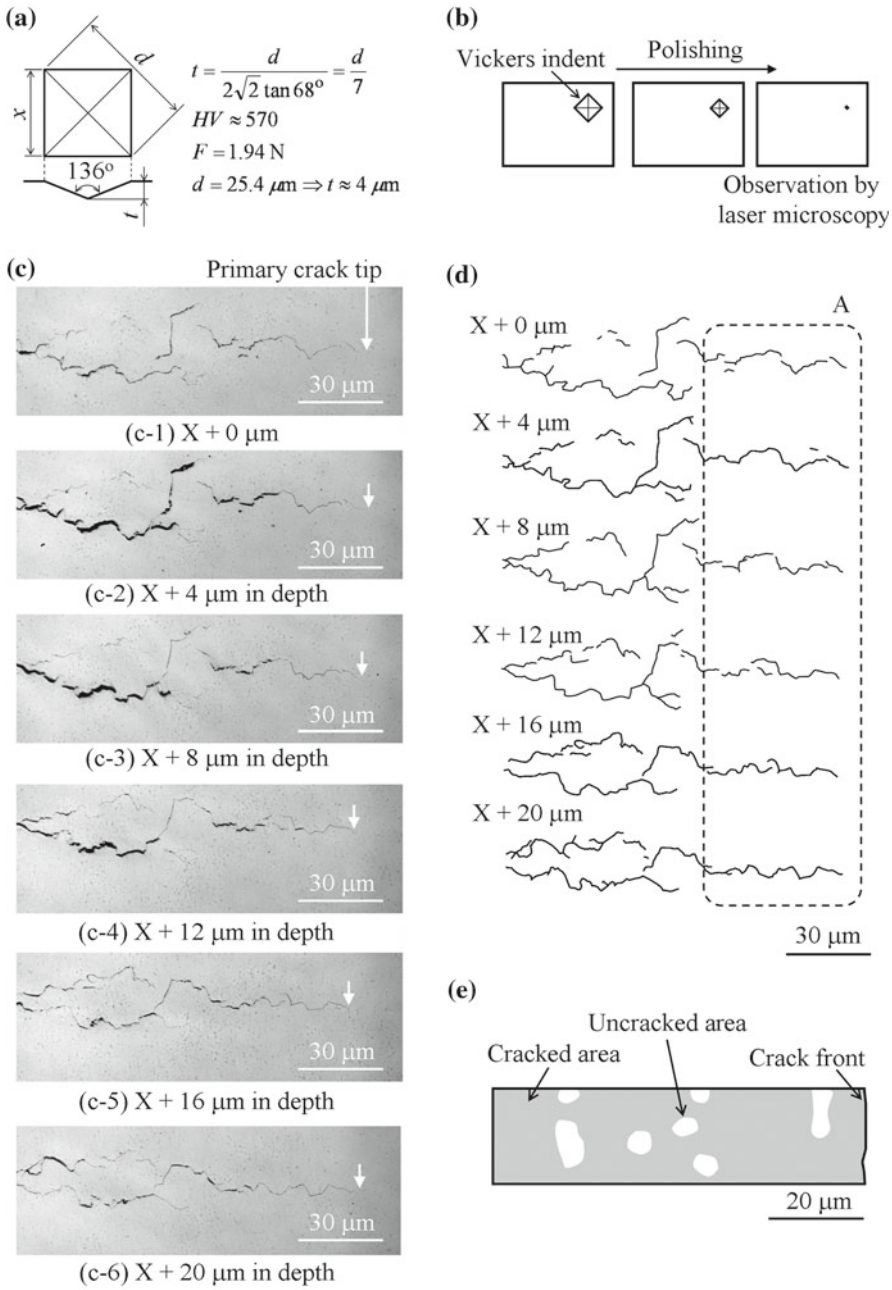


**Fig. 16** Fatigue crack morphology in hydrogen-charged specimen ($C_{H,D} = 1.21$ mass ppm, $da/dN \approx 40$ μm/cycle) tested at $f = 0.2$ Hz, $R = 0.1$, $\Delta K = 12.2\,\mathrm{MPa \cdot m^{1/2}}$: (**a**) schematic illustration of Vickers indent; (**b**) observation method for fatigue crack at each plane by laser microscopy; (**c**) fatigue crack morphology at each plane; (**d**) schematic illustration of (**c**); (**e**) three-dimensional morphology of fatigue crack shape

Surface polishing by an unknown depth (X) compared with the plane in Fig.10 has already been performed before successive polishing

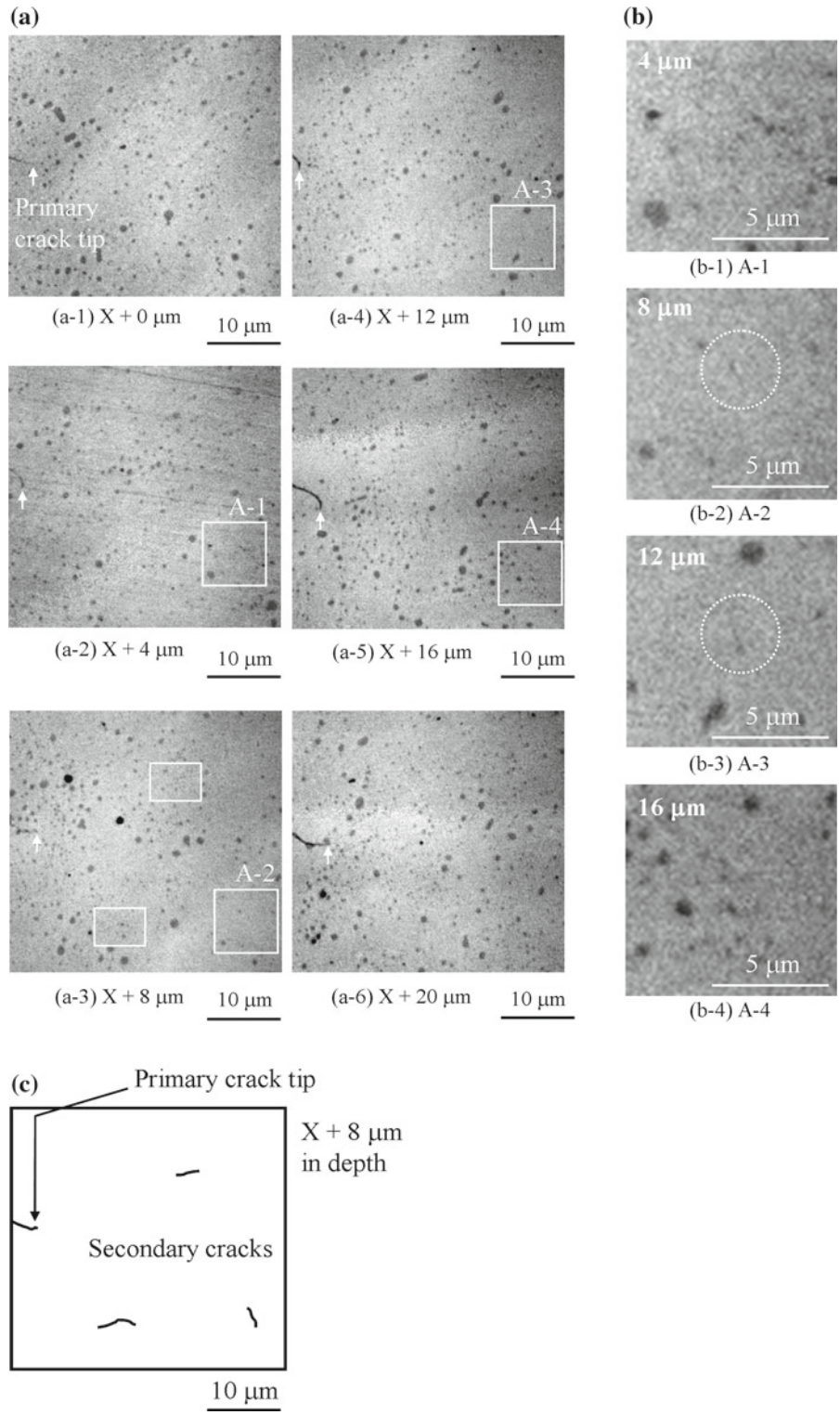


**Fig. 17** Three secondary cracks in hydrogen-charged specimen ($C_{H,D} = 1.21$ mass ppm, d$a$/d$N \approx 40$ μm/cycle) tested at $f = 0.2$ Hz, $R = 0.1$, $\Delta K = 12.2\,\mathrm{MPa \cdot m^{1/2}}$: (**a**) laser micrographs at each plane; (**b**) magnified micrographs of A-1 to A-4 in (**a**); (**c**) location of three isolated cracks in (a-3)

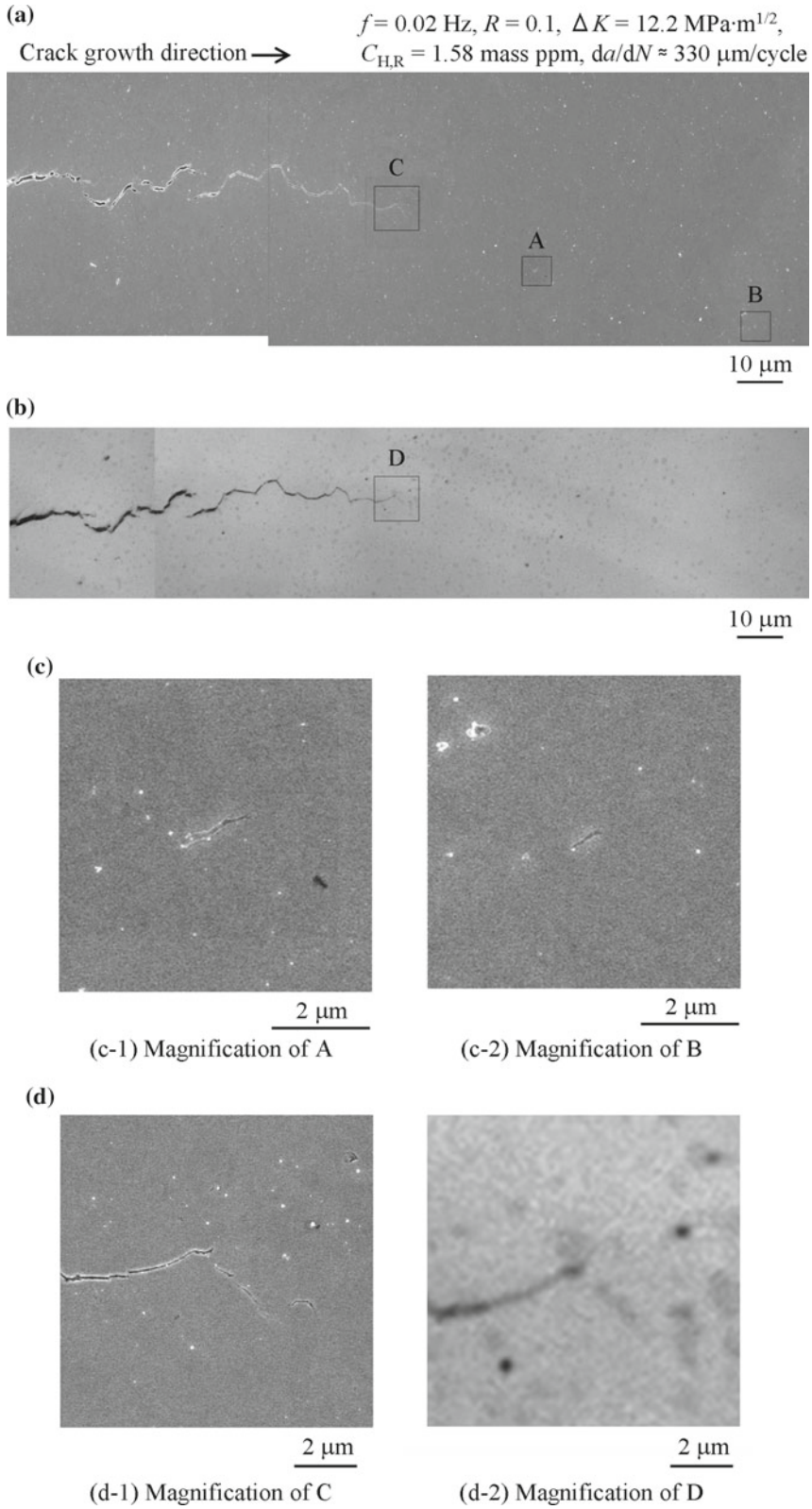


**Fig. 18** SEM and laser micrographs of secondary cracks at the middle section of hydrogen-charged specimen ($C_{H,D}$ = 1.58 mass ppm, d$a$/d$N$ ≈ 330 μm/cycle) tested at $f$ = 0.02 Hz, $R$ = 0.1, $\Delta K$ = 12.2 MPa · m$^{1/2}$: **a** low-magnified SEM macrograph; **b** low-magnified laser micrograph; **c** magnified SEM micrographs of A and B; **d** magnified SEM and laser micrographs of C and D

**Acknowledgments** This research was supported by the NEDO Fundamental Research Project on Advanced Hydrogen Science (2006–2012). The authors gratefully acknowledge the support of the International Institute for Carbon-Neutral Energy Research (WPI-$I^2$CNER), sponsored by the Japanese Ministry of Education, Culture, Sport, Science and Technology. The authors are grateful to Dr. S. Fujita of NSK Corporation for his assistance with part of the experiments. The authors would like to thank Prof. P. Sofronis at University of Illinois, the director of International Institute for Carbon Neutral Energy Research at Kyushu University, Japan, Prof. I. Robertson at University of Illinois, USA, Dr. BP. Somerday at Sandia National Laboratory, USA and Prof. RO. Ritchie at University of California, Berkeley, USA, for their useful discussions and suggestions on the mechanism of secondary crack initiation and deformation twinning. The authors thank Dr. S. Lyth at International Institute for Carbon Neutral Energy Research, Kyushu University, for checking the English manuscript.

## Appendix A: Three-dimensional (3D) morphology of fatigue crack

In order to investigate the three-dimensionally complicated morphology of the fatigue crack shown in Fig. 10, several parallel planes along the primary crack front were observed. Several planes were observed by polishing the surfaces. The depth of their planes was determined from the Vickers indents as shown in Fig. 16a, b. Figure 16c shows the fatigue crack morphology at each plane observed by laser microscopy. Figure 16d is the illustration of Fig. 16c. All the cracks of Fig. 16c termed as the secondary cracks are connected to the primary crack. Figure 16e illustrates the three-dimensional morphology of the fatigue crack shape for hydrogen-charged specimens. It is presumed that the fatigue crack in the hydrogen-charged specimen has a three-dimensionally complicated shape, and several cracks appear isolated from the primary crack. Therefore, the zone ahead of these cracks was more carefully observed.

Figure 17 shows three isolated cracks ahead of the primary crack. Since the successive polishing was applied, the observation was made by laser microscopy which shows less resolution compared with SEM (see Fig. 18d-1, d-2). However, three secondary cracks, which are completely isolated from the primary crack, are observed ahead of the primary crack.

Figure 18 shows SEM and laser macrographs of secondary cracks at the middle section of hydrogen-charged specimen ($C_{H,D} = 1.58$ mass ppm, $da/dN \approx 330\,\mu$m/cycle) tested at $f = 0.02$ Hz, $R = 0.1$, $\Delta K = 12.2\,\mathrm{MPa}\cdot\mathrm{m}^{1/2}$. Because of low resolution of laser

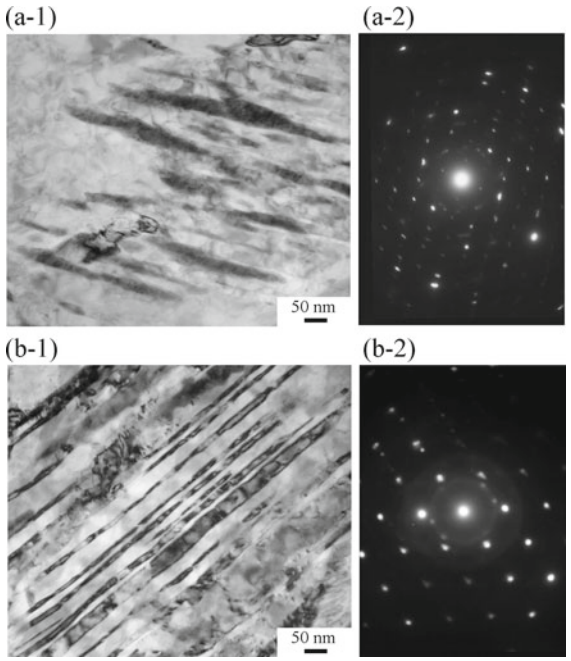


**Fig. 19** TEM micrographs of uncharged specimen before fatigue test: **a-1** TEM micrograph of example 1; **a-2** selected area diffraction pattern of (**a-1**); **b-1** TEM micrograph of example 2; **b-2** selected area diffraction pattern of (**b-1**)

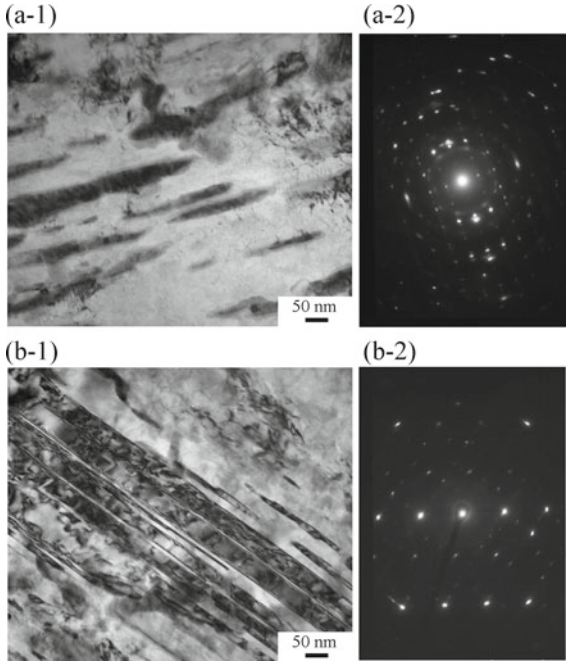


**Fig. 20** TEM micrographs of hydrogen-charged specimen before fatigue test: **a-1** TEM micrograph of example 1; **a-2** selected area diffraction pattern of (**a-1**); (**b-1**) TEM micrograph of example 2; **b-2** selected area diffraction pattern of (**b-1**)

microscopy, the primary crack tip by laser microscopy in Fig. 18d-2 was not clear compared with that by SEM in Fig. 18d-1. Secondary cracks were observed ahead of the primary crack as well as those in Fig. 17.

## Appendix B: TEM observation of uncharged and hydrogen-charged specimens before fatigue test

TEM observations for uncharged and hydrogen-charged specimens before fatigue test were made. Thin specimens for the TEM observations were prepared by electropolishing. The total observation area was about 100 μm × 100 μm. Figures 19 and 20 show TEM micrographs of the uncharged and hydrogen-charged specimens before fatigue test. Although some band structures were observed in the uncharged and hydrogen-charged specimens, the selected diffraction patterns identify that these structures are not twins.

## References


Astafurova EG, Zakharova GG, Maier HJ (2010) Hydrogen-induced twinning in < 111 > Hadfield steel single cystals. Scr Mater 63:1189–1192

ASTM E647 (2010) Standard test method for measurement of fatigue crack growth rates. Annual Book of ASTM Standards

Au JJ, Birnbaum HK (1973) Magnetic relaxation studies of hydrogen in iron: relaxation spectra. Scr Metall 7:595–604

Bandyopadhyay N, Kameda J, McMahon CJ Jr (1983) Hydrogen-induced cracking in 4340-type steel: effects of composition, yield strength, and $H_2$ pressure. Metall Trans 14: 881–888

Beachem CD (1972) A new model for hydrogen-assisted cracking (hydrogen "embrittlement"). Metall Trans 3:437–451

Bechtle S, Kumar M, Somerday BP, Launey ME, Ritchie RO (2009) Grain-boundary engineering markedly reduces susceptibility to intergranular hydrogen embrittlement in metallic materials. Acta Mater 57:4148–4157

Benson RB Jr, Dann RK, Roberts LW Jr (1968) Hydrogen embrittlement of stainless steel. Trans Metall Soc AIME 242:2199–2205

Birnbaum HK, Sofronis P (1994) Hydrogen-enhanced localized plasticity: a mechanism for hydrogen-related fracture. Mater Sci Eng 176:191–202

Birnbaum HK, Robertson IM, Sofronis P (2000) Hydrogen effects on plasticity. In: Lepinoux J (ed) Multiscale phenomena in plasticity. KluwerAcademic Publishers, Dordrecht pp 210–221

Brass AM, Chene J (1998) Influence of deformation on the hydrogen behavior in iron and nickel base alloys: a review of experimental data. Mater Sci Eng 242:210–221

Chandler WT, Walter RJ (1974) Testing to determine the effect of high-pressure hydrogen environments on the mechanical properties of metals. In: Raymond L (ed) Hydrogen embrittlement testing. ASTM STP543, ASTM International pp 170–197

Chandler WT, Walter RJ (1975) Hydrogen-environmental embrittlement of metals and its control. In: Veziroglu TH (ed) Proceedings of the hydrogen Miami energy conference. Plenum Press, New York pp 1057–1078

Cialone H, Asaro RJ (1979) The role of hydrogen in the ductile fracture of plain carbon steels. Metall Mater Trans 10:367–375

Clum JA (1975) The role of hydrogen in dislocation generation in iron alloys. Scr Metall 9:51–58

Dufresne F, Seeger A, Groh P, Moser P (1976) Hydrogen relaxation in a-iron. Phys Status Solidi 36:579–589

Eliezer D, Chakrapani DG, Altstetter CJ, Pugh EN (1979) The influence of austenite stability on the hydrogen embrittlement and stress-corrosion cracking of stainless steel. Metall Mater Trans 10:935–941

Endo K, Komai K, Fujimoto T, Matsuda Y (1980) Environmentally enhanced fatigue crack growth of a high-strength steel sensitive to stress corrosion cracking. Bull JSME 23:807–814

Farrell K, Quarrell AG (1964) Hydrogen embrittlement of an ultra-high-tensile steel. J Iron Steel Inst 302:1002–1011

Ferreira PJ, Robertson IM, Birnbaum HK (1998) Hydrogen effects on the interaction between dislocations. Acta Mater 46:1749–1957

Fujita T, Yamada Y (1977) Physical metallurgy and SCC high strength steels. In: Staehle RW, Hochmann J, McCright RD, Slater JE (eds) Stress corrosion cracking and hydrogen embrittlement of iron base alloys, NACE-5. National Association of Corrosion Engineers, Texas pp 736–746

Gangloff RP (2003) Hydrogen assisted cracking of high strength alloy. In: Milne I, Ritchie RO, Karihaloo B (eds in chief) and Petit J, Scott P (eds in volume) Comprehensive structural integrity. Elsevier Science, New York, pp 31–101

Garber R, Bernstein IM, Thompson AW (1976) Effect of hydrogen on ductile fracture of spheroidized steel. Scr Metall 10:341–345

Gilbert A, Hahn GT, Reid CN, Wilcox BA (1964) Twin-induced grain boundary cracking in b.c.c. metals. Acta Metall 12:754–755

Hahn GT, Bhargava V, Chen Q (1990) The cyclic stress–strain properties, hysteresis loop shape, and kinematic hardening of two high-strength bearing steels. Metall Trans 21:653–665

Hayakawa M, Terasaki S, Hara T, Tsuzaki K, Matsuoka S (2002) Microstructural analyses of modified-ausformed medium-carbon steel with high resistance to hydrogen embrittlement by atomic force microscopy. J Jpn Inst Met 66:745–753

Heller WR (1961) Quantum effects in diffusion: internal friction due to hydrogen and deuterium dissolved in/cap alpha/-iron. Acta Metall 9:600–613

Hirth JP (1980) Effects of hydrogen on the properties of iron and steel. Metall Mater Trans 11:861–890

Hwang C, Bernstein IM (1982) Hydrogen induced slip and twinning in iron alloys. Scr Metall 16:85–90

Jagannadham K, Armstrong RW, Hirth JP (1993) Deformation twinning in high-hydrogen-solubility refractory alloy crystals. Phil Mag 68:419–451

Kameda J, McMahon CJ Jr (1980) Solute segregation and brittle fracture in an alloy steel. Metall Trans 11:91–101
Kameda J, Jokl ML (1982) Dynamic model of hydrogen-induced intergranular cracking. Scr Metall 16:325–330
Kameda J, McMahon CJ Jr (1983) Soltue segregation and hydrogen-induced intergranular fracture in an alloy steel. Metall Trans 14:903–911
Kanezaki T, Narazaki C, Mine Y, Matsuoka S, Murakami Y (2008) Effects of hydrogen on fatigue crack growth behavior of austenitic stainless steels. Int J Hydrogen Energy 33:2604–2619
Kimura H, Matsui H (1979) Reply to "further discussion on the lattice hardening due to dissolved hydrogen in iron and steel" by Asano and Otsuka. Scr Metall 13:221–223
Knop M, Heath J, Sterjovski Z, Lynch SP (2010) Effects of cycle frequency on corrosion-fatigue crack growth in cathodically protected high-strength steels. Procedia Eng 2:1243–1252
Kondo Y, Kubota M, Shimada K (2010) Hydrogen enhanced crack propagation of SCM440H low-alloy steel under long-term varying load. Eng Fract Mech 77:1963–1974
Lagneborg R (1969) Hydrogen embrittlement in austenitic steels and nickel-base alloys. J Iron Steel Inst 207:363–366
Le TD, Bernstein IM, Mahajan S (1993) Effects of hydrogen on micro-twinning in a Fe-Ti-C alloy. Acta Metall Mater 41:3363–3379
Liu HW (2011) Hydrogen assisted intergranular cracking in steels. Eng Fract Mech 78:2563–2571
Macadre A, Yano H, Matsuoka S, Furtado J (2011) The effect of hydrogen on the fatigue life of Ni-Cr -Mo steel envisaged for use as a storage cylinder for a 70 MPa hydrogen station. Int J Fatigue 33:1608–1619
Magnin T, Bosch C, Wolski K, Delafosse D (2001) Cyclic plastic deformation behaviour of Ni single crystals oriented for single slip as a function of hydrogen content. Mater Sci Eng 314(A):7–11
Marchi CS, Somerday BP (2008) Technical reference on hydrogen compatibility of materials. Sandia Rep 1212:1–19
Matsui H, Kimura H, Kimura A (1979) The effect of hydrogen on the mechanical properties of high-purity iron. III. — the dependence of softening on specimen size and charging current density. Mater Sci Eng 40:227–234
Matsuo T, Matsuoka S, Murakami Y (2010) Fatigue crack growth properties of quenched and tempered Cr-Mo steel in 0.7 MPa hydrogen Gas. In: Proceedings of the 18th European conference on fracture, CD-ROM
Matsuo T, Yamabe J, Matsuoka S, Murakami Y (2009) Influence of hydrogen and prestrain on tensile properties of type 316L austenitic stainless steel. In: Somerday BP, Sofronis P, Jones R (eds) Effect of hydrogen on materials. ASM International, Ohio pp 105–112
Matsuoka S, Takeuchi E, Hayakawa M (2010) Improvement of hydrogen fatigue resistance in ferritic steels. In: Proceedings of international hydrogen energy development forum, international HYDROGENIUS symposium, hydrogen-materials interaction, pp 25–33
Matsuoka S, Tanaka H, Homma N, Murakami Y (2011) Influence of hydrogen and frequency on fatigue crack growth behavior of Cr-Mo steel. Int J Fract 168:101–112
McMahon CJ Jr (2001) Hydrogen-induced intergranular fracture of steels. Eng Fract Mech 68:773–788
Mignot F, Doquet V, Sarrazin-Baudoux C (2004) Contributions of internal hydrogen and room—temperature creep to the abnormal fatigue cracking of Ti6246 at high Kmax. Mater Sci Eng 380:308–319
Murakami Y, editor-in-chief (1987) Stress intensity factors handbook, vol 1. Pergamon Press, Oxford, pp 24–26
Murakami Y, Ueda T, Nomoto T, Murakami Y, Ohori M (1999) Analysis of the mechanism of superlong fatigue failure by optical microscope and SEM/AFM observations. J Soc Mater Sci Jpn 48:1112–1117
Murakami Y, Konishi H, Takai K, Murakami Y (2000) Acceleration of superlong fatigue failure by hydrogen trapped by inclusions and elimination of conventional fatigue limit. Tetsu Hagane 86:777–783
Murakami Y (2002) Metal fatigue: effects of small defects and nonmetallic inclusions. Elsevier, Oxford
Murakami Y, Kanezaki T, Mine Y, Matsuoka S (2008) Hydrogen embrittlement mechanism in fatigue of austenitic stainless steel. Metall Mater Trans 39:1327–1339
Murakami Y, Kanezaki T, Mine Y (2010) Hydrogen effect against hydrogen embrittlement. Metall Mater Trans 41: 2548–2562
Murakami Y, Matsuoka S (2010) Effect of hydrogen on fatigue crack growth of metals. Eng Fract Mech 77:1926–1940
Nagumo M, Nakamura M, Takai K (2001) Hydrogen thermal desorption relevant to delayed-fracture susceptibility of high-strength steels. Metall Mater Trans 32:339–347
Novak P, Yuan R, Somerday BP, Sofronis P, Ritchie RO (2010) A statistical, physical-based, micro-mechanical model of hydrogen-induced intergranular fracture in steel. J Mech Phys Solids 58:206–226
Oriani OA, Josephic PH (1974) Equilibrium aspects of hydrogen-induced cracking of steels. Acta Metall 22:1065–1074
Rigsbee JM, Benson RB (1977) A TEM invenstigation of hydrogen-induced deformation twinning and associated martensitic phases in 304-type strainless steel. J Mater Sci lett 12:406–409
Robertson IM, Birnbaum HK (1986) An HVEM study of hydrogen effects on the deformation and fracture of nickel. Acta Metall 34:353–366
Rosenthal Y, Marc-Markowitch M, Stern A, Eliezer D (1981) The influence of hydrogen on the plastic flow and fracture behavior of 316L stainless steel. Scr Metall 15:861–866
Rozenak P, Robertson IM, Birnbaum HK (1990) HVEM studies of the effects of hydrogen on the deformation and fracture of AISI type 316 austenitic stainless steel. Acta Metall Mater 38:2031–2040
Sandoz G (1972) A unified theory for some effects of hydrogen source, alloying/elements, and potential on crack growth in martensitic AISI 4340 steel. Metall Trans 3:1169–1176
Senkov ON, Jonas JJ (1996) Dynamic strain aging and hydrogen-induced softening in alpha titanium. Metall Mater Trans 27:1877–1887
Shih DS, Robertson IM, Birnbaum HK (1988) Hydrogen embrittlement of alpha titanium: in situ TEM studies. Acta Metall 36:111–124
Singh S, Altstetter C (1982) Effects of hydrogen concentration on slow crack growth in stainless steels. Metall Mater Trans 13:1799–1808

Smith RW, Hirschberg MH, Manson SS (1963) Fatigue behavior of materials under strain cycling in low and intermediate life range. NASA Technical Note, D-1574

Sofronis P, McMeeking RM (1989) Numerical analysis of hydrogen transport near a blunting crack tip. J Mech Phys Solids 37:317–350

Somerday BP, March CS (2008) Effect of hydrogen gas on steel vessels and pipelines. In: Jones RH, Thomas GJ (eds) Materials for the hydrogen economy. CRC press, Boca Raton pp 157–179

Stoltz RE, Moody NR, Perra MW (1983) Microfracture model for hydrogen embrittlement of austenitic steels. Metall Mater Trans 14:1528–1531

Suresh S, Ritchie RO (1982) Mechanistic dissimilarities between environmentally-influenced fatigue crack propagation at nearthreshold and higher growth rates in lower strength steels. Metal Sci 16:529–538

Tabata T, Birnbaum HK (1983) Direct observations of the effect of hydrogen on the behavior of dislocations in iron. Scr Metall 17:947–950

Takai K, Watanuki R (2003) Hydrogen in trapping states innocuous to environmental degradation of high-strength steels. ISIJ Int 43:520–526

Tau L, Chan SLI, Shin CS (1996) Hydrogen enhanced fatigue crack propagation of bainitic and tempered martensitic steels. Corrs Sci 38:2049–2060

Toplosky J, Ritchie RO (1981) On the influence of gaseous hydrogen in decelerating fatigue crack growth rates in ultrahigh strength steels. Scr Metall 15:905–908

Troiano AR (1960) The role of hydrogen and other interstitials in the mechanical behavior of metals. Trans ASM 52:54–80

Valiente A, Caballero L, Ruiz J (1999) Hydrogen assisted failure of precracked specimens of 316L stainless steel. Nucl Eng Des 188:203–216

Vennett RM, Ansell GS (1967) The effect of high-pressure hydrogen upon the tensile orioertues and fracture behavior of 304L stainless steel. Trans ASM Q 60:242–251

Walter RJ, Chandler WT (1968) Effect of high-pressure hydrogen on metals. The 1968 materials engineering exposition and congress, ASM

Wei RP, Landes JD (1969) Correlation between sustained-load and fatigue crack growth in high-strength steels. Mater Res Stand 9:25–46

Wei RP, Simmons GW (1981) Recent progress in understanding environmental assisted fatigue crack growth. Int J Fract 17:235–247

Yano H, Homma N, Fukushima Y, Macadre A, Furutado J, Matsuoka S (2010) Effects of hydrogen and test frequency on fatigue properties of JIS-SNCM439 steel for storage cylinder of 70 MPa hydrogen station. Trans Jpn Soc Mech Eng 76:918–927

Yoshikawa M, Tsutsumi N, Matsuoka S, Murakami Y (2010) Effect of hydrogen pressure and test frequency on fatigue crack growth of a ferrite-pearlite steel in hydrogen gas. Trans Jpn Soc Mech Eng 76:908–917

Yoshino K, McMahon CJ Jr (1974) The cooperative relation between temper embrittlement and hydrogen embrittlement in a high strength steel. Metall Trans 5:363–370